SIAM J. SCI. COMPUT.
Vol. 42, No. 6, pp. A3932–A3956

FIFTH-ORDER A-WENO FINITE-DIFFERENCE SCHEMES BASED ON A NEW ADAPTIVE DIFFUSION CENTRAL NUMERICAL FLUX*

BAO-SHAN WANG†, WAI SUN DON†, NAVEEN K. GARG‡, AND ALEXANDER KURGANOV§

Abstract. A new adaptive diffusion central numerical flux within the framework of fifth-order characteristicwise alternative WENO-Z finite-difference schemes (A-WENO) with a modified local Lax–Friedrichs (LLF) flux for the Euler equations of gas dynamics is introduced. The new numerical flux adaptively adjusts the numerical diffusion coefficient present in the LLF flux. The coefficient is estimated by a suitable Rankine–Hugoniot condition, which gives a more accurate estimation of the local speed of propagation. To ensure robustness, lower and upper bounds of the coefficient are obtained with the help of the convection-pressure splitting of the Jacobian. The proposed adaptive A-WENO scheme is tested on several one- and two-dimensional benchmarks. The obtained results demonstrate that the use of the adaptive diffusion central numerical flux enhances the resolution of contact waves and improves significantly the resolution of fine-scale structures in the smooth areas of the solution while capturing shocks and high gradients in an essentially nonoscillatory manner.

Key words. A-WENO schemes, central schemes, Rankine–Hugoniot condition

AMS subject classifications. 65M06, 76M20, 65M08, 76M12, 76N15, 76L05, 35L65

DOI. 10.1137/20M1327926

1. Introduction.

This paper is focused on numerical solutions of hyperbolic systems of conservation laws. In the one-dimensional (1-D) case, these systems read as

$$\boldsymbol{U}_t + \boldsymbol{F}(\boldsymbol{U})_x = \boldsymbol{0}. \tag{1.1}$$

It is well-known that solutions of (1.1) may develop complicated wave structures that include shock waves, rarefactions, and contact discontinuities even when the initial data are smooth. It is, therefore, quite challenging to develop highly accurate, stable, and robust numerical methods, which are supposed to have a sufficient (but not too large) amount of numerical diffusion (ND) needed to stabilize computed solutions. Finite-volume Godunov-type schemes are a popular tool that may achieve the goal; see, e.g., the monographs [11, 18, 22, 31]. In the framework of Godunov-type schemes, the solution is represented using its cell averages, which are used to obtain a global in space (generically discontinuous) piecewise polynomial reconstruction needed to

*Submitted to the journal's Methods and Algorithms for Scientific Computing section March 27, 2020; accepted for publication (in revised form) September 28, 2020; published electronically December 14, 2020.

https://doi.org/10.1137/20M1327926

Funding: The work of the first and second authors was partially supported by the Ocean University of China through grant 201712011. The work of the third author was partially supported by SUSTech through grant Y01031300. The work of the fourth author was partially supported by NSFC through grant 11771201 and by the fund of the Guangdong Provincial Key Laboratory of Computational Science and Material Design through grant 2019B030301001.

†School of Mathematical Sciences, Ocean University of China, Qingdao, 266100, China (wbs@stu.ouc.edu.cn, donwaisun@outlook.com).

‡Corresponding author. Department of Mathematics, Southern University of Science and Technology, Shenzhen, 518055, China, and IISc Mathematics Initiative (IMI), Indian Institute of Science, Bangalore, 560012, India (garg.naveen70@gmail.com).

§Department of Mathematics and SUSTech International Center for Mathematics, Southern University of Science and Technology, Shenzhen, 518055, China (alexander@sustech.edu.cn).

evolve the cell averages in time using the integral form of the studied system of conservation laws.

There are two popular classes of Godunov-type schemes: *upwind* and *central* ones. The first-order upwind scheme is the Godunov scheme [12], which is based on a first-order piecewise constant reconstruction and upwinding utilized by solving the Riemann problems initiated at every time step at all of the cell interfaces. The order of upwind methods can be increased by using higher-order piecewise polynomial (say, piecewise linear for second-order schemes) reconstructions. This requires, however, solving the generalized Riemann problems, which is a much more complicated task; see, e.g., [3]. Nonoscillatory central schemes offer a much simpler alternative to the upwind ones. Godunov-type central schemes are constructed by shifting the space-time control volumes in space in such a manner that the computed solution is averaged over the Riemann fans so that no (generalized) Riemann problem solver is needed for time evolution. The simplest Godunov-type central scheme is the staggered Lax–Friedrichs scheme, whose order (and resolution) can be increased using proper piecewise polynomial reconstructions; see [36], where the second-order staggered central scheme was proposed.

Staggered central schemes, however, have quite large ND due to their staggered grid structure. The amount of ND can be reduced by utilizing the information about local speeds of propagation and making the spatial size of space-time control volumes to be proportional to these speeds. This was done in [27], where second-order nonstaggered central schemes were developed. The simplest version of these schemes is the semidiscrete central scheme, whose first-order version coincides with the Rusanov scheme [39], which is often referred to as a local Lax–Friedrichs (LLF) scheme. Compared to their staggered counterparts, the nonstaggered central schemes are less diffusive and thus more accurate. Moreover, they are more robust as their ND coefficients are not inversely proportional to the size of the time step; see [27] for details.

The accuracy of semidiscrete central schemes is determined by the order of the piecewise polynomial reconstruction employed to compute the point values of $\boldsymbol{U}$, needed to evaluate the numerical fluxes, and the order of the ODE solver used for the time evolution. Third-order semidiscrete central schemes were derived in [25]. Higher-order schemes can be obtained using higher-order ENO (see, e.g., [15, 16, 44, 45]) and WENO (see, e.g., [2, 4, 20, 35, 43]) reconstructions. Schemes that utilize ENO (WENO) reconstructions are often referred to as ENO (WENO) schemes. These schemes may be based on any numerical flux, but they are often based on the simplest central (LLF) flux, which is very robust. Though the LLF flux is less accurate than Riemann-problem-solver-based upwind fluxes, a very high accuracy is typically achieved thanks to a very accurate reconstruction.

A drawback of ENO (WENO) schemes is that the reconstruction procedure becomes very complicated and computationally expensive in the multidimensional case. A way to overcome this difficulty is to switch from the finite-volume to the finite-difference scheme, for which a 1-D WENO reconstruction can be performed in every space dimension. The first finite-difference WENO scheme was proposed in [20] and then further developed in [1, 4, 5, 6, 17]. These schemes, however, are based on quite diffusive flux splitting required to stabilize them, and this affects the quality of the obtained results, which are typically not as accurate as the results computed using finite-volume WENO schemes. The way of enhancing the resolution of finite-difference WENO schemes was proposed in [21], where alternative WENO (A-WENO) schemes were developed; also, see [34]. The main advantage of A-WENO schemes is that they can employ standard finite-volume numerical fluxes (without any need in flux splitting and related modifications), whose accuracy, in the context of finite-difference

schemes, is limited to the second order, while a high order is achieved using the flux Taylor expansion.

A-WENO schemes have been typically implemented using the LLF numerical flux; see [33, 47]. In this paper, we develop an alternative, adaptive diffusion central numerical flux and implement it in the framework of fifth-order A-WENO schemes. The new numerical flux is based on the central Rankine–Hugoniot (R-H) schemes, which were derived in [10, 19, 38]. These schemes utilize the R-H conditions at a discrete level. This allows such schemes to capture steady discontinuities accurately, but the central R-H schemes from [10, 19, 38] are not robust enough. Here, we consider the Euler equations of gas dynamics and utilize the convection-pressure (C-P) flux splitting from [49] to develop an adaptive modification of the central R-H flux. The new flux is as robust as the LLF flux, and at the same time, it contains a substantially smaller amount of ND. This is demonstrated on a number of challenging numerical examples for both 1-D and two-dimensional (2-D) Euler equations.

The paper is organized as follows. In section 2, we briefly review the fifth-order A-WENO schemes. In particular, in section 2.1, we describe the fifth-order WENO-Z interpolation, which is used to design the proposed scheme. In section 3, we provide a brief overview of semidiscrete central schemes and describe the central (LLF) flux, which is modified in section 4, where we derive the new adaptive diffusion central flux. In section 5, we present both 1-D (section 5.1) and 2-D (section 5.2) numerical examples. Some concluding remarks can be found in section 6. Finally, the C-P flux splitting used in the derivation of the proposed adaptive numerical flux is described in Appendix A.

2. The fifth-order A-WENO schemes: A brief overview. We consider the 1-D system (1.1) on a certain interval covered with the uniform cells $I_j := [x_{j-\frac{1}{2}}, x_{j+\frac{1}{2}}]$ of size Δx centered at $x_j = (x_{j-\frac{1}{2}} + x_{j+\frac{1}{2}})/2$. Assuming that the point values $\boldsymbol{U}_j(t) \approx \boldsymbol{U}(x_j, t)$ have been already computed at a certain time level t (for the sake of brevity, we will omit the time dependence of all of the indexed quantities in most parts in the rest of this paper). These point values are then evolved in time according to the following semidiscretization:

$$\frac{\mathrm{d}}{\mathrm{d}t}\boldsymbol{U}_j = -\frac{\boldsymbol{\mathcal{F}}_{j+\frac{1}{2}} - \boldsymbol{\mathcal{F}}_{j-\frac{1}{2}}}{\Delta x}, \tag{2.1}$$

where $\boldsymbol{\mathcal{F}}_{j+\frac{1}{2}}$ are numerical fluxes, which are supposed to be designed in a way that would make the right-hand side (RHS) of (2.1) to be equal to $\boldsymbol{F}(\boldsymbol{U}(x_j,t))_x + \mathcal{O}\big((\Delta x)^5\big)$ for smooth solutions.

According to the A-WENO approach (see [21, 33, 47]), the fifth-order numerical flux is obtained using the sixth-order accurate Taylor expansion of $\boldsymbol{\mathcal{F}}(x)$ at $x = x_{j+\frac{1}{2}}$ (see [44]) given by

$$\boldsymbol{\mathcal{F}}_{j+\frac{1}{2}} = \boldsymbol{\mathcal{F}}^{\mathrm{FV}}_{j+\frac{1}{2}} - \frac{1}{24}(\Delta x)^2(\boldsymbol{F}_{xx})_{j+\frac{1}{2}} + \frac{7}{5760}(\Delta x)^4(\boldsymbol{F}_{xxxx})_{j+\frac{1}{2}}. \tag{2.2}$$

Here, $\boldsymbol{\mathcal{F}}^{\mathrm{FV}}_{j+\frac{1}{2}}$ is the finite-volume numerical flux, which, in the case of the LLF flux and its proposed modification, presented in sections 3 and 4, respectively, is a function of the left- and right-sided point values of $\boldsymbol{U}$ at $x = x_{j+\frac{1}{2}}$. These one-sided point values, denoted by $\boldsymbol{U}^-_{j+\frac{1}{2}}$ and $\boldsymbol{U}^+_{j+\frac{1}{2}}$, respectively, are obtained using the WENO-Z interpolation procedure [21, 33, 47], described in section 2.1.

In order to ensure that the numerical flux in (2.2) is fifth-order accurate, the approximations of the second and fourth derivatives of the flux $\boldsymbol{F}$ are computed using the standard central finite differences of the fourth and the second order, respectively:

$$(\boldsymbol{F}_{xx})_{j+\frac{1}{2}} = \frac{1}{48(\Delta x)^2}\left(-5\boldsymbol{F}_{j-2} + 39\boldsymbol{F}_{j-1} - 34\boldsymbol{F}_j - 34\boldsymbol{F}_{j+1} + 39\boldsymbol{F}_{j+2} - 5\boldsymbol{F}_{j+3}\right),$$

$$(\boldsymbol{F}_{xxxx})_{j+\frac{1}{2}} = \frac{1}{2(\Delta x)^4}\left(\boldsymbol{F}_{j-2} - 3\boldsymbol{F}_{j-1} + 2\boldsymbol{F}_j + 2\boldsymbol{F}_{j+1} - 3\boldsymbol{F}_{j+2} + \boldsymbol{F}_{j+3}\right),$$

where $\boldsymbol{F}_j := \boldsymbol{F}(\boldsymbol{U}_j)$.

2.1. The fifth-order WENO-Z interpolation. We now review the fifth-order WENO-Z interpolation (see [7, 9, 21, 32, 33, 47]), which is used to compute the one-sided point values $\boldsymbol{U}^{\pm}_{j+\frac{1}{2}}$ required to evaluate the finite-volume numerical fluxes $\boldsymbol{\mathcal{F}}^{\rm FV}_{j+\frac{1}{2}}$. In fact, we will only describe how to compute $\boldsymbol{U}^{-}_{j+\frac{1}{2}}$, which will be obtained using the stencil $S^5 := [x_{j-2}, \ldots, x_{j+2}]$, which is biased to the left of $x_{j+\frac{1}{2}}$. The point value $\boldsymbol{U}^{+}_{j+\frac{1}{2}}$ will then be obtained using the mirror-symmetric (with respect to the target point $x_{j+\frac{1}{2}}$) stencil.

One can perform either a componentwise or, preferably, a characteristicwise interpolation. In the former case, we denote by $Q := U^{(m)}$ the mth component of the conservative variable vector $\boldsymbol{U}$. In the latter case, $Q := (L\boldsymbol{U})^{(m)}$ is the mth component of the characteristic variable vector $L\boldsymbol{U}$, where L is a matrix composed of the Roe-averaged left eigenvectors of the Jacobian of the flux function at the cell interface $x_{j+\frac{1}{2}}$; see [21] for details.

Given the point values $\{Q_j\}$, we will consider the three parabolic interpolants $\mathcal{P}_k(x)$ obtained using the three point values Q_{j-2+k}, Q_{j-1+k}, and Q_{j+k} on the corresponding substencils $S_k := [x_{j-2+k}, x_{j-1+k}, x_{j+k}]$ for $k = 0$, 1, and 2. Then, the fifth-order WENO-Z interpolation procedure gives

$$Q^{-}_{j+\frac{1}{2}} = \sum_{k=0}^{2} \omega_k \mathcal{P}_k(x_{j+\frac{1}{2}}),$$

where

$$\begin{aligned}
\mathcal{P}_0(x_{j+\frac{1}{2}}) &= \frac{3}{8}Q_{j-2} - \frac{5}{4}Q_{j-1} + \frac{15}{8}Q_j,\\
\mathcal{P}_1(x_{j+\frac{1}{2}}) &= -\frac{1}{8}Q_{j-1} + \frac{3}{4}Q_j + \frac{3}{8}Q_{j+1},\\
\mathcal{P}_2(x_{j+\frac{1}{2}}) &= \frac{3}{8}Q_j + \frac{3}{4}Q_{j+1} - \frac{1}{8}Q_{j+2}.
\end{aligned}$$

The (nonlinear) weights ω_k of the fifth-order WENO-Z interpolant are obtained as follows (see [4, 5, 6]):

$$\alpha_k = d_k\left[1 + \left(\frac{\tau_5}{\beta_k + \varepsilon}\right)^p\right], \quad \omega_k = \frac{\alpha_k}{\alpha_0 + \alpha_1 + \alpha_2}.$$

Here, $d_0 = 1/16$, $d_1 = 5/8$, and $d_2 = 5/16$ are the linear (optimal) weights, which yield the (optimal) fifth-order accuracy for a smooth function;

$$\beta_k = \sum_{\ell=1}^{2}(\Delta x)^{2\ell-1}\int_{x_{j-\frac{1}{2}}}^{x_{j+\frac{1}{2}}}\left(\frac{\partial^\ell \mathcal{P}_k}{\partial x^\ell}\right)^2 {\rm d}x, \quad k = 0, 1, 2,$$

are the (local lower order) smoothness indicators, which measure the smoothness of $Q(x)$ in each substencil (the explicit expressions for the smoothness indicators β_k can be found in [4, 20, 21]); $\tau_5 = |\beta_2 - \beta_0|$ is the global (optimal order) smoothness indicator, which has a leading truncation error of order $\mathcal{O}\big((\Delta x)^5\big)$; p is the power parameter; and $\varepsilon > 0$ is the sensitivity parameter used to avoid a division by zero. In all of the numerical experiments presented in section 5, we have used $\varepsilon = 10^{-12}$ and $p = 2$.

We note that if $Q(x)$ is a smooth function in the stencil S^5, then the smoothness indicators β_k, $k = 1, 2, 3$, are all of about the same order and one can easily verify that in this case, $Q^-_{j+\frac{1}{2}} = Q(x_{j+\frac{1}{2}}) + \mathcal{O}\big((\Delta x)^5\big)$. At the same time, if a substencil S_k contains a discontinuity, the corresponding β_k will be much larger than those of other two smooth substencils, and hence the associated weight α_k will be correspondingly much smaller than the others and will tend to zero, which would lead to a second-order and smoother biased polynomial approximation. This way, an essentially non-oscillatory property of the WENO-Z interpolation procedure is achieved.

Remark 1. Even though the componentwise WENO interpolation is essentially nonoscillatory, the resulting A-WENO scheme may still be prone to some numerical oscillations. As demonstrated in [37], these types of oscillations can be greatly reduced by performing the interpolation in the local characteristic variables rather than in the original, conservative ones. In all of the numerical examples presented in section 5, the characteristicwise WENO-Z interpolation is used to compute the $\boldsymbol{U}^{\pm}_{j+\frac{1}{2}}$.

3. Semidiscrete central schemes: A brief overview. In this section, a brief description of the semidiscrete finite-volume central schemes for (1.1) from [27] is given. These schemes are based on the finite-volume central fluxes $\boldsymbol{\mathcal{F}}^{\mathrm{FV}}_{j+\frac{1}{2}}$, which are the key ingredients of the A-WENO schemes studied here; see (2.2).

As in all finite-volume methods, the computed solution is realized in terms of its cell averages $\overline{\boldsymbol{U}}_j(t) \approx \frac{1}{\Delta x}\int_{I_j} \boldsymbol{U}(x,t)\,\mathrm{d}x$. They are assumed to be known at a given time t and are then evolved in time according to the following central semidiscretization rigorously derived in [27]:

$$\frac{\mathrm{d}}{\mathrm{d}t}\overline{\boldsymbol{U}}_j = -\frac{\boldsymbol{\mathcal{F}}^{\mathrm{FV}}_{j+\frac{1}{2}} - \boldsymbol{\mathcal{F}}^{\mathrm{FV}}_{j-\frac{1}{2}}}{\Delta x}, \tag{3.1}$$

where

$$\boldsymbol{\mathcal{F}}^{\mathrm{FV}}_{j+\frac{1}{2}} = \frac{1}{2}\left[\boldsymbol{F}\left(\boldsymbol{U}^-_{j+\frac{1}{2}}\right) + \boldsymbol{F}\left(\boldsymbol{U}^+_{j+\frac{1}{2}}\right)\right] - \frac{1}{2}a_{j+\frac{1}{2}}\Delta\boldsymbol{U}_{j+\frac{1}{2}}, \quad \Delta\boldsymbol{U}_{j+\frac{1}{2}} := \boldsymbol{U}^+_{j+\frac{1}{2}} - \boldsymbol{U}^-_{j+\frac{1}{2}}, \tag{3.2}$$

are the numerical fluxes. The accuracy of the numerical flux (3.2) is determined by the accuracy of the piecewise polynomial reconstruction employed to evaluate $\boldsymbol{U}^{\pm}_{j+\frac{1}{2}}$; see, e.g., [23] and references therein. Finally, the ND coefficient $a_{j+\frac{1}{2}}$ in (3.2) is the maximum local speed of propagation, which is obtained from the spectral radius of the Jacobian $A(\boldsymbol{U}) = \frac{\partial \boldsymbol{F}}{\partial \boldsymbol{U}}$.

For example, let us consider the Euler equations of gas dynamics, which in the 1-D case read as

$$\begin{aligned} &\rho_t + (\rho u)_x = 0,\\ &m_t + (\rho u^2 + p)_x = 0,\\ &E_t + ((E+p)u)_x = 0. \end{aligned} \tag{3.3}$$

Here, ρ is the density of the fluid, u is the velocity, $m=\rho u$ is the momentum, p is the pressure, E is the total energy, which is a sum of internal and kinetic energies given by $E=\frac{p}{\gamma-1}+\frac{1}{2}\rho u^2$, and γ is the ratio of specific heats, which is constant in the case of ideal gas. In order to design the central scheme for (3.3), the point values $\rho^{\pm}_{j+\frac{1}{2}}$, $m^{\pm}_{j+\frac{1}{2}}$, and $E^{\pm}_{j+\frac{1}{2}}$ at the cell boundary $x_{j+\frac{1}{2}}$ are interpolated and the ND coefficient $a_{j+\frac{1}{2}}$ is estimated by

$$a_{j+\frac{1}{2}}=\max\left\{\left|u^{+}_{j+\frac{1}{2}}\right|+c^{+}_{j+\frac{1}{2}},\left|u^{-}_{j+\frac{1}{2}}\right|+c^{-}_{j+\frac{1}{2}}\right\}, \tag{3.4}$$

where $c:=\sqrt{\gamma p/\rho}$ is the speed of sound and

$$u^{\pm}_{j+\frac{1}{2}}=\frac{m^{\pm}_{j+\frac{1}{2}}}{\rho^{\pm}_{j+\frac{1}{2}}},\quad c^{\pm}_{j+\frac{1}{2}}=\sqrt{\frac{\gamma p^{\pm}_{j+\frac{1}{2}}}{\rho^{\pm}_{j+\frac{1}{2}}}},\quad p^{\pm}_{j+\frac{1}{2}}=(\gamma-1)\left[E^{\pm}_{j+\frac{1}{2}}-\frac{\left(m^{\pm}_{j+\frac{1}{2}}\right)^2}{2\rho^{\pm}_{j+\frac{1}{2}}}\right]. \tag{3.5}$$

4. Adaptive diffusion central flux. In this section, we derive an adaptive diffusion modification of the central (LLF) flux (3.2), (3.4), (3.5) for the compressible Euler equations (3.3). Our goal is to reduce the ND by replacing the ND coefficient $a_{j+\frac{1}{2}}$ given by (3.4) with a smaller adaptive ND coefficient $\alpha_{j+\frac{1}{2}}$, which will represent a more accurate estimate on the maximum local speeds of propagation without solving the generalized Riemann problem or trying to incorporate any upwinding information. The adaptive LLF numerical flux,

$$\boldsymbol{\mathcal{F}}^{\mathrm{FV}}_{j+\frac{1}{2}}=\frac{1}{2}\left[\boldsymbol{F}\left(\boldsymbol{U}^{-}_{j+\frac{1}{2}}\right)+\boldsymbol{F}\left(\boldsymbol{U}^{+}_{j+\frac{1}{2}}\right)\right]-\frac{1}{2}\alpha_{j+\frac{1}{2}}\Delta\boldsymbol{U}_{j+\frac{1}{2}}, \tag{4.1}$$

is designed using a suitable discrete R-H condition and the C-P flux splitting described in Appendix A. Based on the considered flux splitting, we first split the numerical flux into the convection and pressure parts as follows:

$$\boldsymbol{\mathcal{F}}^{\mathrm{FV}}_{j+\frac{1}{2}}=\boldsymbol{\mathcal{F}}^{\mathrm{c}}_{j+\frac{1}{2}}+\boldsymbol{\mathcal{F}}^{\mathrm{p}}_{j+\frac{1}{2}},$$

where

$$\mathcal{F}^{\ell,(i)}_{j+\frac{1}{2}}=\frac{1}{2}\left[F^{\,\ell,(i)}\left(\boldsymbol{U}^{-}_{j+\frac{1}{2}}\right)+F^{\,\ell,(i)}\left(\boldsymbol{U}^{+}_{j+\frac{1}{2}}\right)\right]-\frac{1}{2}\alpha^{\ell}_{j+\frac{1}{2}}\Delta U^{(i)}_{j+\frac{1}{2}},\quad \ell\in\{\mathrm{c},\mathrm{p}\}, \tag{4.2}$$

for the ith component of the numerical fluxes $\boldsymbol{\mathcal{F}}^{\mathrm{c}}_{j+\frac{1}{2}}$ and $\boldsymbol{\mathcal{F}}^{\mathrm{p}}_{j+\frac{1}{2}}$. Our main goal is to evaluate $\alpha^{\mathrm{c}}_{j+\frac{1}{2}}$ and $\alpha^{\mathrm{p}}_{j+\frac{1}{2}}$ in (4.2). Once this is done, we will use an appropriate discrete R-H condition along with (A.3) to obtain $\alpha_{j+\frac{1}{2}}=\alpha^{\mathrm{c}}_{j+\frac{1}{2}}+\alpha^{\mathrm{p}}_{j+\frac{1}{2}}$ in (4.1).

Let us assume that the data at time t locally at $x=x_{j+\frac{1}{2}}$ corresponds to either an isolated shock or a contact discontinuity propagating to the right. In this case, the convection part of the numerical flux would capture steady isolated discontinuities exactly if $\mathcal{F}^{\mathrm{c,(i)}}_{j+\frac{1}{2}}=F^{\,\mathrm{c,(i)}}\big(\boldsymbol{U}^{-}_{j+\frac{1}{2}}\big)$ in (4.2), which results in

$$\Delta F^{\mathrm{c,(i)}}_{j+\frac{1}{2}}=\alpha^{\mathrm{c}}_{j+\frac{1}{2}}\Delta U^{(i)}_{j+\frac{1}{2}}\quad\forall i,\quad\text{where}\quad\Delta F^{\mathrm{c,(i)}}_{j+\frac{1}{2}}:=F^{\,\mathrm{c,(i)}}\left(\boldsymbol{U}^{+}_{j+\frac{1}{2}}\right)-F^{\,\mathrm{c,(i)}}\left(\boldsymbol{U}^{-}_{j+\frac{1}{2}}\right). \tag{4.3}$$

Hence, for these special data we can obtain $\alpha^{\mathrm{c}}_{j+\frac{1}{2}}$ from (4.3),

$$\alpha^{\mathrm{c}}_{j+\frac{1}{2}}=\frac{\Delta F^{\mathrm{c,(i)}}_{j+\frac{1}{2}}}{\Delta U^{(i)}_{j+\frac{1}{2}}}, \tag{4.4}$$

and it will be independent of i. This, however, is not true for general data, for which formula (4.4) cannot be used. Therefore, in order to be able to handle the general data case, we use the third (energy E) component of the fluxes by taking $i = 3$ in (4.4). This choice is motivated by the fact that the energy contains the contribution of both the kinetic and internal energies and hence carries maximum information of propagation of waves. We thus set

$$\alpha^{\mathrm{c}}_{j+\frac{1}{2}} = \frac{\Delta F^{\mathrm{c},(3)}_{j+\frac{1}{2}}}{\Delta E_{j+\frac{1}{2}}}, \quad \Delta F^{\mathrm{c},(3)}_{j+\frac{1}{2}} := F^{\mathrm{c},(3)}\left(\boldsymbol{U}^{+}_{j+\frac{1}{2}}\right) - F^{\mathrm{c},(3)}\left(\boldsymbol{U}^{-}_{j+\frac{1}{2}}\right). \tag{4.5}$$

Applying similar arguments to the pressure part of the numerical flux gives

$$\alpha^{\mathrm{p}}_{j+\frac{1}{2}} = \frac{\Delta F^{\mathrm{p},(3)}_{j+\frac{1}{2}}}{\Delta E_{j+\frac{1}{2}}}, \quad \Delta F^{\mathrm{p},(3)}_{j+\frac{1}{2}} := F^{\mathrm{p},(3)}\left(\boldsymbol{U}^{+}_{j+\frac{1}{2}}\right) - F^{\mathrm{p},(3)}\left(\boldsymbol{U}^{-}_{j+\frac{1}{2}}\right). \tag{4.6}$$

Adding (4.5) and (4.6) up and using once again the flux splitting (A.3) result in

$$\alpha_{j+\frac{1}{2}} = \frac{\Delta F^{\mathrm{c},(3)}_{j+\frac{1}{2}}}{\Delta E_{j+\frac{1}{2}}} + \frac{\Delta F^{\mathrm{p},(3)}_{j+\frac{1}{2}}}{\Delta E_{j+\frac{1}{2}}} = \frac{\Delta F^{(3)}_{j+\frac{1}{2}}}{\Delta E_{j+\frac{1}{2}}}, \quad \Delta F^{(3)}_{j+\frac{1}{2}} := F^{(3)}\left(\boldsymbol{U}^{+}_{j+\frac{1}{2}}\right) - F^{(3)}\left(\boldsymbol{U}^{-}_{j+\frac{1}{2}}\right). \tag{4.7}$$

Similarly for a left-going isolated shock or contact discontinuity, we will obtain

$$\alpha_{j+\frac{1}{2}} = -\frac{\Delta F^{(3)}_{j+\frac{1}{2}}}{\Delta E_{j+\frac{1}{2}}}. \tag{4.8}$$

Finally, in order to avoid any directional dependence in (4.1), we combine (4.7) and (4.8) to define the following ND coefficient:

$$\alpha_{j+\frac{1}{2}} = \left|\frac{\Delta F^{(3)}_{j+\frac{1}{2}}}{\Delta E_{j+\frac{1}{2}}}\right|. \tag{4.9}$$

The semidiscrete central scheme (3.1), based on the numerical flux (4.1), (4.9), can capture isolated discontinuities accurately. However, it does not have an appropriate amount of ND as the obtained discrete R-H based ND coefficient (4.9) may be either too small or too large, particularly in the rarefaction regions of the flow fields. Therefore, one needs to bound this ND coefficient in order to ensure that the scheme generates physically realistic discrete solutions. To this end, we require that the coefficients $\alpha^{\mathrm{c}}_{j+\frac{1}{2}}$ and $\alpha^{\mathrm{p}}_{j+\frac{1}{2}}$ fall within the bounds set using the smallest and largest (by magnitude) eigenvalues of the matrices A^{c} and A^{p}, respectively, namely,

$$\min\left\{\left|u^{-}_{j+\frac{1}{2}}\right|, \left|u^{+}_{j+\frac{1}{2}}\right|\right\} \le \alpha^{\mathrm{c}}_{j+\frac{1}{2}} \le \max\left\{\left|u^{-}_{j+\frac{1}{2}}\right|, \left|u^{+}_{j+\frac{1}{2}}\right|\right\},$$
$$0 \le \alpha^{\mathrm{p}}_{j+\frac{1}{2}} \le \max\left\{c^{-}_{j+\frac{1}{2}}, c^{+}_{j+\frac{1}{2}}\right\},$$

and hence,

$$\min\left\{\left|u^{-}_{j+\frac{1}{2}}\right|, \left|u^{+}_{j+\frac{1}{2}}\right|\right\} \le \alpha_{j+\frac{1}{2}} \le \max\left\{\left|u^{-}_{j+\frac{1}{2}}\right|, \left|u^{+}_{j+\frac{1}{2}}\right|\right\} + \max\left\{c^{-}_{j+\frac{1}{2}}, c^{+}_{j+\frac{1}{2}}\right\}. \tag{4.10}$$

Notice that the upper bound in (4.10) is larger than the original upper bound on the local speeds (3.4), which was obtained based on the spectral radius of the unsplit matrix A. In order to further reduce the amount of ND, the upper bound in (4.10) is replaced with $a_{j+\frac{1}{2}}$ given by (3.4). We, therefore, expect the resulting scheme to be stable provided

(4.11)
$$\alpha^{\min}_{j+\frac{1}{2}} := \min\left\{\left|u^-_{j+\frac{1}{2}}\right|, \left|u^+_{j+\frac{1}{2}}\right|\right\} \le \alpha_{j+\frac{1}{2}} \le \max\left\{\left|u^-_{j+\frac{1}{2}}\right| + c^-_{j+\frac{1}{2}}, \left|u^+_{j+\frac{1}{2}}\right| + c^+_{j+\frac{1}{2}}\right\} =: \alpha^{\max}_{j+\frac{1}{2}}.$$

Our adaptive diffusion central scheme is designed by modifying (4.9) in such a way that the stability ensuring inequality (4.11) is satisfied. In particular, we take the adaptive ND coefficient

$$\alpha_{j+\frac{1}{2}} = \begin{cases} \min\left\{\alpha^{\min}_{j+\frac{1}{2}}, \kappa\,\alpha^{\max}_{j+\frac{1}{2}}\right\} & \text{if } \theta_{j+\frac{1}{2}} \le (\Delta x)^2, \\ \max\left\{\alpha^{\min}_{j+\frac{1}{2}}, \min\left(\widehat{\alpha}_{j+\frac{1}{2}}, \alpha^{\max}_{j+\frac{1}{2}}\right)\right\} & \text{otherwise,} \end{cases} \tag{4.12}$$

where the smoothness detector $\theta_{j+\frac{1}{2}}$ is defined as

$$\theta_{j+\frac{1}{2}} = \max_{1\le i\le 3}\left\{\frac{\left|\Delta U^{(i)}_{j+\frac{1}{2}}\right|}{\max\left(\left|(U^{(i)})^+_{j+\frac{1}{2}}\right|, \left|(U^{(i)})^-_{j+\frac{1}{2}}\right|, \delta\right)}\right\}.$$

Here, $\mathbf{U} := (\rho, m, E)^\top$ is the conservative variable, and $\widehat{\alpha}_{j+\frac{1}{2}}$ denotes the following desingularized version of (4.9):

$$\widehat{\alpha}_{j+\frac{1}{2}} = \frac{2\left|\Delta F^{(3)}_{j+\frac{1}{2}}\right|}{\left|\Delta E_{j+\frac{1}{2}}\right| + \max\left\{\left|\Delta E_{j+\frac{1}{2}}\right|, \delta\right\}}, \tag{4.13}$$

where $\delta > 0$ is a small desingularization parameter (in all of the numerical experiments reported in section 5, we have used $\delta = 10^{-10}$), and $\kappa \in [0, 1]$ is a numerical diffusion regulator (NDR) number, whose role will be discussed in section 5.

In summary, the resulting adaptive diffusion central flux $\boldsymbol{\mathcal{F}}^{\mathrm{FV}}_{j+\frac{1}{2}}$, which will be used in the construction of the fifth-order finite-difference numerical flux in (2.2), is

$$\boldsymbol{\mathcal{F}}^{\mathrm{FV}}_{j+\frac{1}{2}} = \frac{1}{2}\left[\boldsymbol{F}\left(\boldsymbol{U}^-_{j+\frac{1}{2}}\right) + \boldsymbol{F}\left(\boldsymbol{U}^+_{j+\frac{1}{2}}\right)\right] - \frac{1}{2}\alpha_{j+\frac{1}{2}}\Delta\boldsymbol{U}_{j+\frac{1}{2}}, \quad \Delta\boldsymbol{U}_{j+\frac{1}{2}} := \boldsymbol{U}^+_{j+\frac{1}{2}} - \boldsymbol{U}^-_{j+\frac{1}{2}},$$

where

$$\alpha_{j+\frac{1}{2}} = \begin{cases} \min\left\{\alpha^{\min}_{j+\frac{1}{2}}, \kappa\,\alpha^{\max}_{j+\frac{1}{2}}\right\} & \text{if } \theta_{j+\frac{1}{2}} \le (\Delta x)^2, \\ \max\left\{\alpha^{\min}_{j+\frac{1}{2}}, \min\left(\widehat{\alpha}_{j+\frac{1}{2}}, \alpha^{\max}_{j+\frac{1}{2}}\right)\right\} & \text{otherwise,} \end{cases}$$

with

$$\alpha^{\min}_{j+\frac{1}{2}} = \min\left\{\left|u^-_{j+\frac{1}{2}}\right|, \left|u^+_{j+\frac{1}{2}}\right|\right\}, \quad \alpha^{\max}_{j+\frac{1}{2}} = \max\left\{\left|u^-_{j+\frac{1}{2}}\right| + c^-_{j+\frac{1}{2}}, \left|u^+_{j+\frac{1}{2}}\right| + c^+_{j+\frac{1}{2}}\right\},$$

$$\theta_{j+\frac{1}{2}} = \max_{1\le i\le 3}\left\{\frac{\left|\Delta U^{(i)}_{j+\frac{1}{2}}\right|}{\max\left(\left|(U^{(i)})^+_{j+\frac{1}{2}}\right|, \left|(U^{(i)})^-_{j+\frac{1}{2}}\right|, \delta\right)}\right\}, \quad \widehat{\alpha}_{j+\frac{1}{2}} = \frac{2\left|\Delta F^{(3)}_{j+\frac{1}{2}}\right|}{\left|\Delta E_{j+\frac{1}{2}}\right| + \max\left\{\left|\Delta E_{j+\frac{1}{2}}\right|, \delta\right\}}.$$

Remark 2. The desingularization used in (4.13) is just one of the possible desingularization procedures. Several alternatives were discussed, for example, in [24, 26] in the context of computing velocities in shallow water models. Furthermore, when the density is small, a similar desingularization may be needed in computing $u^{\pm}_{j+\frac{1}{2}}$ and $c^{\pm}_{j+\frac{1}{2}}$ in (3.5).

Remark 3. In the first line in the adaptive diffusion central flux (4.12), we check whether the solution is locally smooth by the smoothness detector $\theta_{j+\frac{1}{2}}$, and add only a small amount of ND there. The smoothness criterion is based on the relative smallness of $\left|\Delta U^{(i)}_{j+\frac{1}{2}}\right|$, which is supposed to be proportional to $(\Delta x)^5$ for smooth solutions interpolated using the fifth-order WENO-Z interpolant. The threshold of $(\Delta x)^2$ there is selected experimentally.

Remark 4. The proposed A-WENO scheme can be extended to hyperbolic systems of balance laws,

$$\boldsymbol{U}_t + \boldsymbol{F}(\boldsymbol{U})_x = \boldsymbol{S}(\boldsymbol{U}),$$

in a straightforward way. The modified semidiscretization (2.1) will then read as

$$\frac{\mathrm{d}}{\mathrm{d}t}\boldsymbol{U}_j = -\frac{\boldsymbol{\mathcal{F}}_{j+\frac{1}{2}} - \boldsymbol{\mathcal{F}}_{j-\frac{1}{2}}}{\Delta x} + \boldsymbol{S}(\boldsymbol{U}_j),$$

where the numerical fluxes $\boldsymbol{\mathcal{F}}_{j+\frac{1}{2}}$ are obtained precisely in the same way as in the sourceless case.

5. Numerical examples. In this section, we present several 1-D and 2-D numerical examples. Our main goal is to demonstrate that the use of the adaptive diffusion central flux (section 4) in (2.2) leads to higher-resolution—yet very robust—A-WENO schemes compared with the one obtained by using the LLF flux (section 3). The studied numerical fluxes will be referred to as ADAPTIVE and LLF fluxes, and the obtained solutions will be referred to as ADAPTIVE and LLF solutions, respectively. The 2-D finite-difference A-WENO schemes on Cartesian meshes are designed in a "dimension-by-dimension" approach; see, e.g., [33]. Notice that the 2-D extension is quite simple since, in the finite-difference framework, WENO-Z reconstructions are performed in each direction separately using the point values of the computed solution at the grid points. The ratio of specific heats is taken to be $\gamma = 1.4$ in Examples 1–8 and $\gamma = 5/3$ in Example 9. In all of the presented examples, the time evolution has been carried out using the three-stage third-order strong stability preserving Runge–Kutta solver (see, e.g., [13, 14]) with the CFL number 0.45.

5.1. One-dimensional examples. We begin with the 1-D examples. In all of them, we take three different values of NDR, $\kappa = 0.5$, 0.2, and 0.1, which ensures that in the areas of smooth parts of the computed solutions, the adaptive ND coefficient $\alpha_{j+\frac{1}{2}}$ in the ADAPTIVE flux is smaller than the ND coefficient $a_{j+\frac{1}{2}}$ in the LLF flux.

Example 1—Slowly moving isolated contact discontinuity. We consider the initial conditions,

$$(\rho(x,0), u(x,0), p(x,0)) = \begin{cases} (1.4, 0.1, 1), & x < 0.3, \\ (1.0, 0.1, 1), & x > 0.3, \end{cases}$$

which correspond to an isolated moving contact discontinuity, across which $\Delta F^{(3)} = u\Delta E$.

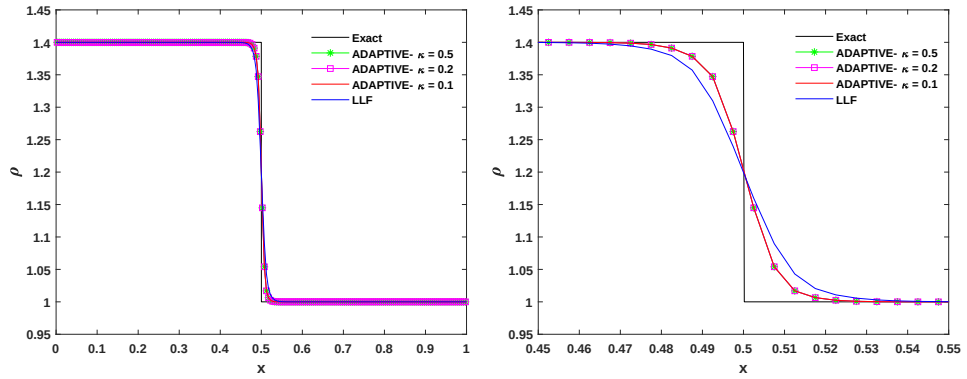

FIG. 5.1. *Example* 1*: Density* (ρ) *computed using the ADAPTIVE and LLF fluxes (left) and zoom at the contact discontinuity area (right).*

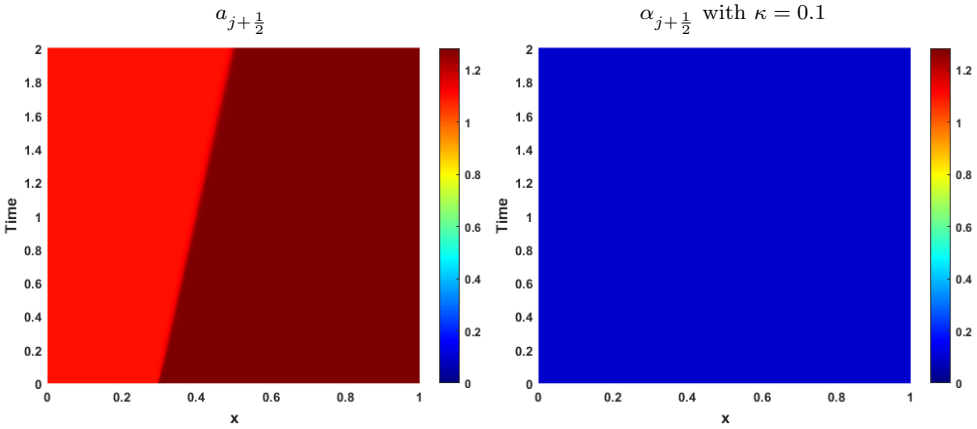

FIG. 5.2. *Example* 1*: Time evolution of* $a_{j+\frac{1}{2}}$ *(left) and* $\alpha_{j+\frac{1}{2}}$ *(right).*

We compute the ADAPTIVE and LLF solutions until the final time $t = 2$ on a uniform grid with $\Delta x = 1/200$. The obtained densities are shown in Figure 5.1, where one can see that the ADAPTIVE solutions for different values of κ are essentially the same, and they are sharper than the LLF solution. The corresponding ND coefficients, $\alpha_{j+\frac{1}{2}}$ (for $\kappa = 0.1$) and $a_{j+\frac{1}{2}}$, as functions of time are plotted in Figure 5.2. As one can see, $\alpha_{j+\frac{1}{2}} \equiv 0.1$, which is the speed of the moving contact discontinuity $u = 0.1$, while $a_{j+\frac{1}{2}} \approx 1.1$ are substantially larger.

Example 2—Lax problem. We consider the Riemann initial data,

$$(\rho(x,0), u(x,0), p(x,0)) = \begin{cases} (0.445, 0.698, 3.528), & x < 0, \\ (0.500, 0.000, 0.571), & x > 0, \end{cases}$$

which is a variant of the Lax problem from [29]. We compute the solution until the final time $t = 1.3$ on a uniform grid with $\Delta x = 1/20$ and plot the densities in Figure 5.3. As in the case of isolated moving contact wave, the ADAPTIVE solutions are slightly sharper than the LLF one in the area of the contact discontinuity, which is zoomed

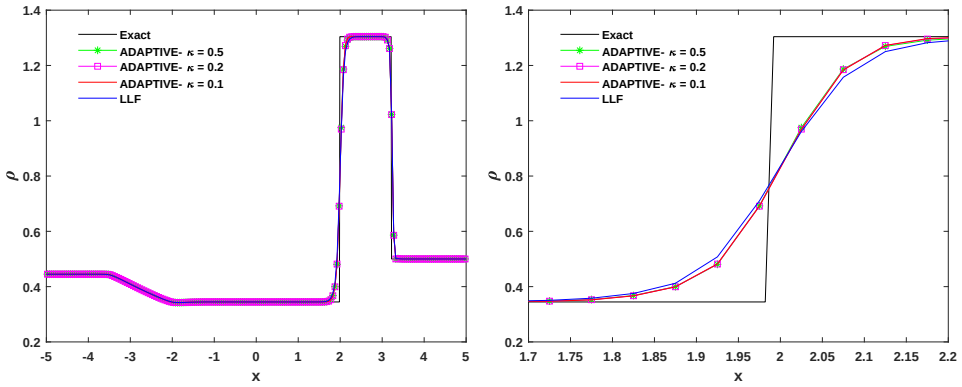

FIG. 5.3. *Example 2: Density (ρ) computed using the ADAPTIVE and LLF fluxes (left) and zoom at the contact discontinuity area (right).*

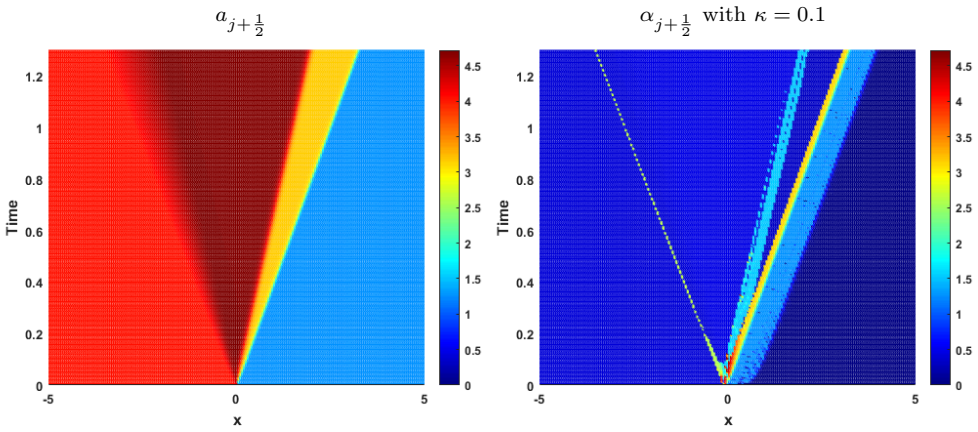

FIG. 5.4. *Example 2: Time evolution of $a_{j+\frac{1}{2}}$ (left) and $\alpha_{j+\frac{1}{2}}$ (right).*

in Figure 5.3 (right). Like in Example 1, the ADAPTIVE solutions are very similar for different values of κ.

In Figure 5.4, the time evolution of the corresponding ND coefficients, $a_{j+\frac{1}{2}}$ and $\alpha_{j+\frac{1}{2}}$, are shown. Here, $\alpha_{j+\frac{1}{2}}$ is roughly equal to $\kappa a_{j+\frac{1}{2}}$ in the areas where the solution is smooth. However, at the left rarefaction corner, along with other areas near discontinuities, the ADAPTIVE flux adds a little more ND. This way of switching makes the ADAPTIVE solution essentially nonoscillatory near the sharp rarefaction corners as well as at and near the discontinuities.

Example 3—Blastwave problem. We consider the strong shocks interaction problem proposed in [48]. The initial conditions,

$$(\rho(x,0),u(x,0),p(x,0)) = \begin{cases} (1,0,1000), & x < 0.1, \\ (1,0,0.01), & 0.1 \le x \le 0.9, \\ (1,0,100), & x > 0.9, \end{cases}$$

are prescribed on the interval $[0,1]$, at both ends of which the reflective boundary conditions are imposed. The final time is $t = 0.038$. We compute the ADAPTIVE

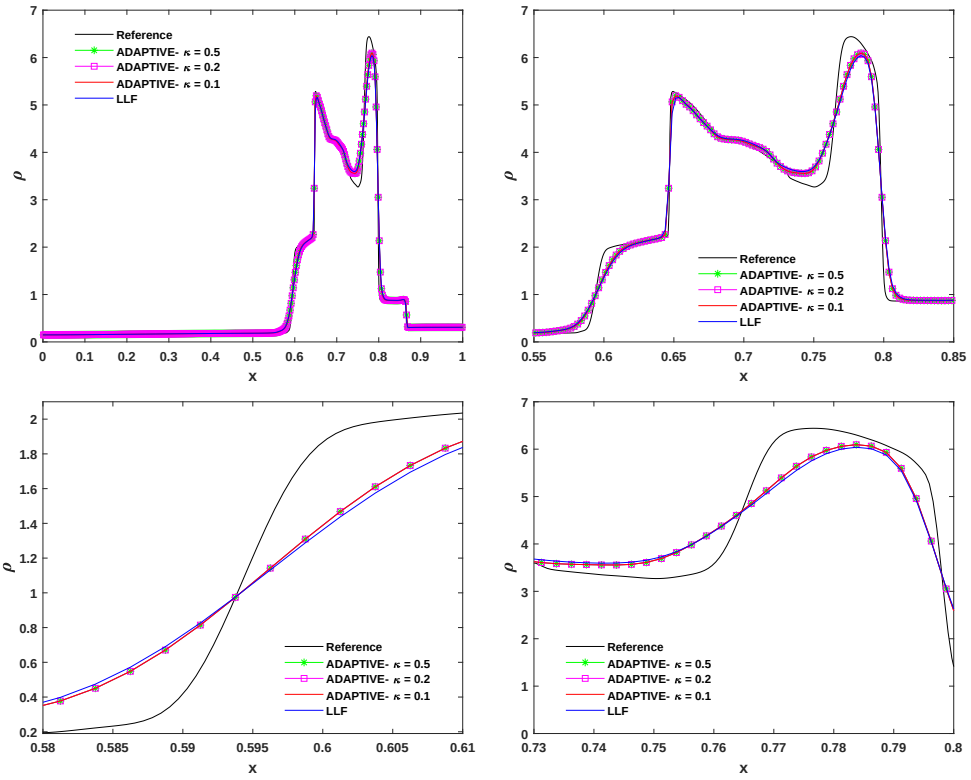

FIG. 5.5. *Example 3: Density (ρ) computed using the ADAPTIVE and LLF fluxes (top left) and zooms at the region of maximum interaction of waves (top right) and two contact discontinuities (bottom row).*

and LLF solutions using $\Delta x = 1/400$ and plot the densities in Figure 5.5. The LLF solution computed using a finer mesh with $\Delta x = 1/1600$ serves as a reference solution. As one can see, the ADAPTIVE solutions are practically identical for different values of κ and are slightly sharper than the LLF solution. From the time evolution of $a_{j+\frac{1}{2}}$ and $\alpha_{j+\frac{1}{2}}$, shown in Figure 5.6, one can see that $\alpha_{j+\frac{1}{2}} \approx \kappa a_{j+\frac{1}{2}}$ in the smooth density region, whereas the switch perfectly maintains the adaptive nature of the scheme in the regions of shock, contact, and rarefaction waves.

Remark 5. We note that the solutions in Examples 1–3 mainly consist of piecewise constant/linear functions. In these examples, we have primarily demonstrated the robustness of the ADAPTIVE flux in capturing high gradients and discontinuities. Its ability to substantially enhance the resolution for long final time due to the adaptive nature of the ADAPTIVE flux will be shown in Examples 4 and 5, where the solutions will contain both shocks/high gradient areas and large fine-scale structures.

Example 4—Shock-density wave interaction problem. We now consider the shock-density wave interaction problem originally proposed in [44] and then slightly modified in [5], where larger computational domain and final time were considered. The initial conditions,

$$(\rho(x,0),u(x,0),p(x,0)) = \begin{cases} (27/7, 4\sqrt{35}/9, 31/3), & x < -4, \\ (1+0.2\sin(5x),0,1), & x > -4, \end{cases}$$

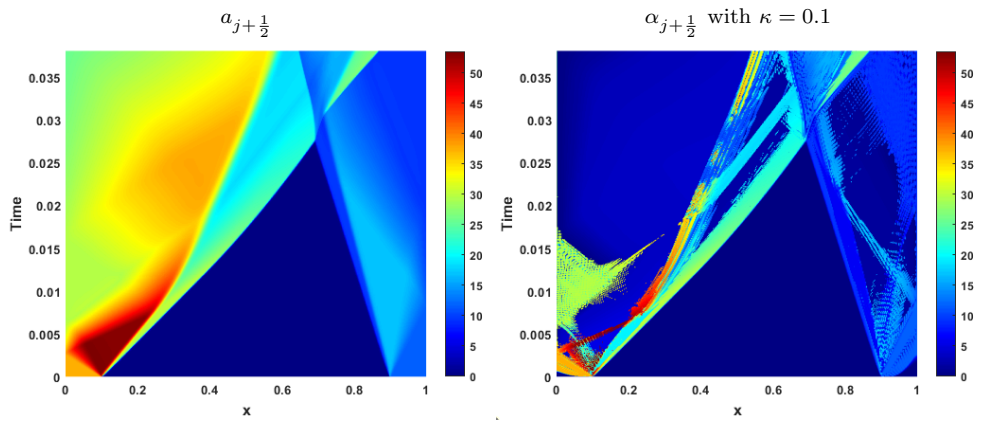

FIG. 5.6. *Example 3: Time evolution of* $a_{j+\frac{1}{2}}$ *(left) and* $\alpha_{j+\frac{1}{2}}$ *(right).*

are prescribed on the interval $[-5, 15]$, at both ends of which we set the free-stream boundary conditions. In this problem, a Mach 3 shock wave interacts with density disturbances created by perturbations present in the initial density. These disturbances then trigger the continuous nonlinear interaction of smooth flow with the discontinuities to generate high-frequency entropy waves along with multiple shocklets downstream.

We compute the ADAPTIVE and LLF solutions until the final time $t = 5$ on a very coarse mesh with $\Delta x = 1/20$. A reference solution is generated using the LLF flux, but on a finer mesh with $\Delta x = 1/80$. The densities are plotted in Figure 5.7, where one can clearly see that the high-frequency waves are better resolved using the ADAPTIVE numerical flux than the LLF one. The shocklets downstream of the main shock are well captured in an essentially nonoscillatory manner due to the larger ND coefficients being utilized in the ADAPTIVE flux. In addition, we now see an influence of the NDR number κ on the quality of the computed solution: smaller values of κ lead to the improved resolution of the high-frequency waves. However, the accuracy of the ADAPTIVE solutions computed with $\kappa = 0.1$ and 0.2 is almost the same and does not improve when κ is further decreased. This suggests that $\kappa = 0.1$ might be a very good choice for the proposed adaptive diffusion central numerical flux.

In Figure 5.8, we show the time evolution of the ND coefficients $a_{j+\frac{1}{2}}$ and $\alpha_{j+\frac{1}{2}}$. As one can see, in most of the domain $\alpha_{j+\frac{1}{2}} = \kappa a_{j+\frac{1}{2}}$. However, $\alpha_{j+\frac{1}{2}}$ and $a_{j+\frac{1}{2}}$ become comparable in the immediate neighborhoods of shock waves. The proposed switch has performed very well in distinguishing between the shock/high gradient and smooth parts of the solution: it self-adjusts to reduce the amount of ND needed to accurately resolve the smooth structures while capturing shocks in an essentially nonoscillatory way.

Furthermore, Figure 5.9 shows the ND coefficients of the blastwave (at $t = 0.038$) and shock-density (at $t = 5$) problems computed using the ADAPTIVE (with $\kappa = 0.1$) and LLF fluxes. The obtained results suggest that the ND coefficients can be substantially reduced without risking spurious oscillation wherever the computed solution is sufficiently smooth.

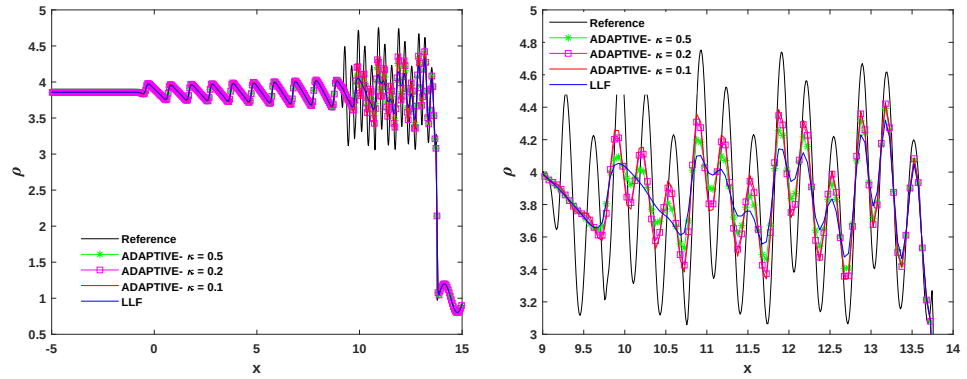

FIG. 5.7. *Example 4: Density (ρ) computed using the ADAPTIVE and LLF fluxes (left) and zoom at the high-frequency entropy waves area (right).*

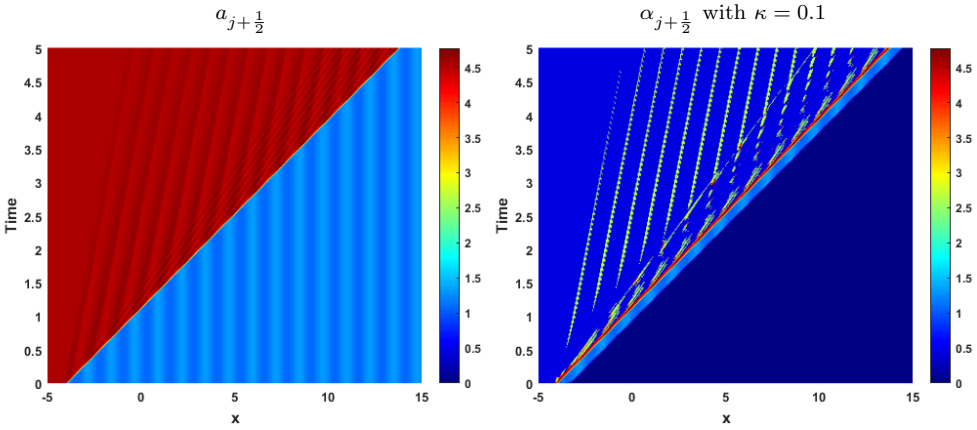

FIG. 5.8. *Example 4: Time evolution of $a_{j+\frac{1}{2}}$ (left) and $\alpha_{j+\frac{1}{2}}$ (right).*

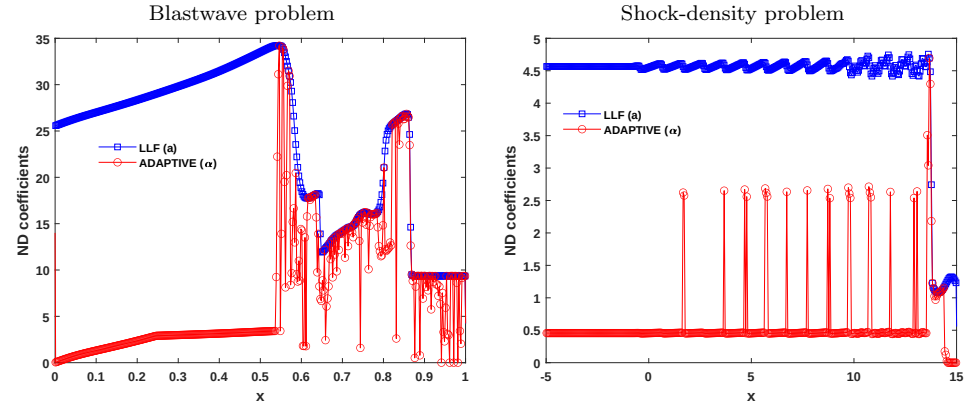

FIG. 5.9. *Examples 3 and 4: ND coefficients for the blastwave problem at $t = 0.038$ (left) and shock-density problem at $t = 5$ (right) computed using the ADAPTIVE and LLF fluxes.*

Example 5—Shock-entropy wave interaction problem. The final 1-D example, taken from [46], can be considered as a variation of the shock-density wave interaction problem (Example 4) with a smaller perturbation amplitude and a weaker shock. The initial conditions,

$$(\rho(x,0),u(x,0),p(x,0)) = \begin{cases} (1.51695, 0.523346, 1.805), & x < -4.5, \\ (1+0.1\sin(20x), 0, 1), & x > -4.5, \end{cases}$$

are prescribed on the interval $[-5,5]$, at both ends of which we set the free-stream boundary conditions. In this problem, a forward-facing shock wave of Mach 1.1 interacts with high-frequency density perturbations: as the shock wave moves, the perturbations spread ahead. It is well-known that the developing high-frequency entropy waves are difficult to accurately resolve. Moreover, these waves typically quickly dissipate further downstream from the main shock under a coarse mesh resolution.

We compute the ADAPTIVE and LLF solutions until the final time $t = 5$ on a coarse mesh with $\Delta x = 1/40$. A reference solution is generated using the LLF flux on a finer mesh with $\Delta x = 1/200$. The densities, plotted in Figure 5.10, clearly demonstrate the superiority of the proposed adaptive diffusion central numerical flux over the LLF one. We also observe that the ADAPTIVE solutions computed with different choices of κ are quite similar. Figure 5.11 shows that $\alpha_{j+\frac{1}{2}}$ is substantially smaller than $a_{j+\frac{1}{2}}$ throughout the entire domain except near the main shock where $\alpha_{j+\frac{1}{2}} \approx a_{j+\frac{1}{2}}$. This allows the smooth high-frequency waves to advect downstream with the amplitude almost unchanged in a long time simulation due to a substantially smaller ND present in the adaptive diffusion central numerical flux.

5.2. Two-dimensional examples. We now consider the 2-D Euler equations of gas dynamics:

$$\begin{aligned} &\rho_t + (\rho u)_x + (\rho v)_y = 0, \\ &m_t + (\rho u^2 + p)_x + (\rho uv)_y = 0, \\ &n_t + (\rho uv)_x + (\rho v^2 + p)_y = 0, \\ &E_t + ((E+p)u)_x + ((E+p)v)_y = 0. \end{aligned}$$

Here, ρ is the density, u and v are the x- and y-velocities, respectively, $m := \rho u$ and $n := \rho v$ are the x- and y-momenta, respectively, p is the pressure, and $E = \frac{p}{\gamma-1} + \frac{1}{2}\rho(u^2+v^2)$ is the total energy.

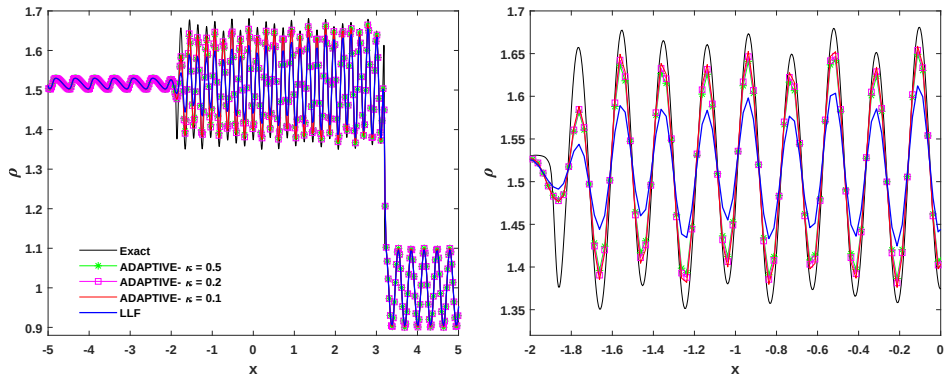

FIG. 5.10. *Example 5: Density (ρ) computed using the ADAPTIVE and LLF fluxes (left) and zoom at the high-frequency entropy waves area (right).*

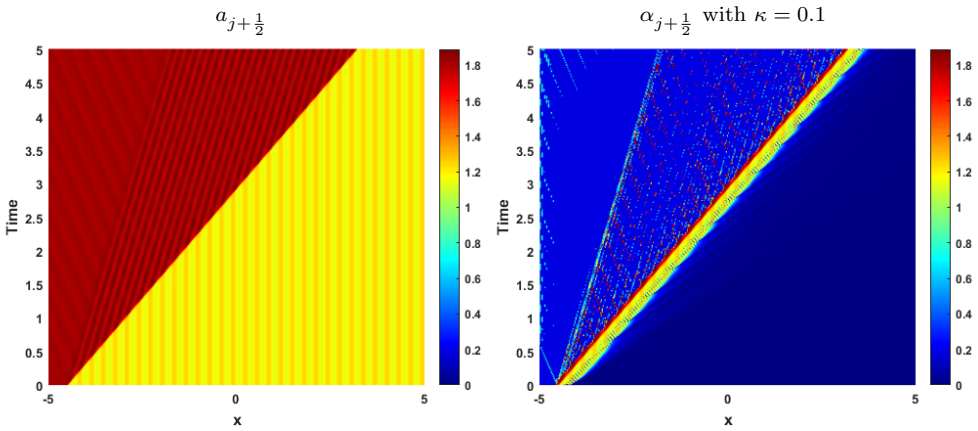

FIG. 5.11. *Example 5: Time evolution of* $a_{j+\frac{1}{2}}$ *(left) and* $\alpha_{j+\frac{1}{2}}$ *(right).*

Based on the 1-D results reported in section 5.1, $\kappa = 0.1$ seems to be a small—yet reliable—NDR number. Therefore, we have taken $\kappa = 0.1$ in all of the 2-D numerical examples reported below.

Example 6—Double Mach reflection. In the first 2-D example taken from [48], we consider the double Mach reflection of a strong shock from an oblique surface. It describes the reflection of a planar Mach shock in the air hitting a wedge. The computational domain is $[0,4] \times [0,1]$ and the initial conditions are

$$(\rho(x,y,0), u(x,y,0), v(x,y,0), p(x,y,0)) = \begin{cases} (8, 8.25\cos\theta, -8.25\sin\theta, 116.5), & x < \frac{1}{6} + \frac{y}{\sqrt{3}}, \\ (1.4, 0, 0, 1), & x > \frac{1}{6} + \frac{y}{\sqrt{3}}, \end{cases}$$

where $\theta = \pi/6$. Supersonic inflow boundary conditions are specified at $x = 0$ and at the short part of the lower boundary $y = 0$ in the interval $x \in [0, 1/6]$, while the remaining part of the lower boundary is assumed to be a solid wall. Free-stream outflow boundary conditions are set at $x = 4$. Finally, at the upper boundary $y = 1$, the exact solution of the Mach 10 moving oblique shock is imposed.

We compute the ADAPTIVE and LLF solutions until the final time $t = 0.2$ on a uniform mesh with $\Delta x = \Delta y = 1/200$. The obtained densities are shown in Figure 5.12, where one can see that the small-scale structures along the slip line and the vortical rollup (the integrity of the mushroom shaped structure) at the tip of the jet are much better resolved in the ADAPTIVE solution. In Figure 5.13, we demonstrate that the ND coefficients of the ADAPTIVE fluxes in both x- and y-directions are substantially smaller than those of the corresponding LLF fluxes in the areas where the solution is sufficiently smooth. One can also observe that the distribution of larger ND coefficients of the ADAPTIVE fluxes agrees well with the locations of shocks, high gradients, and small-scale structures.

Example 7—Forward facing step problem. The forward facing step problem [48] is initialized by a right-going Mach 3 flow in a wind tunnel containing a step. The wind tunnel is 1 length unit wide and 3 length units long. The step is 0.2 length units high and is located 0.6 length units from the left end of the tunnel. Reflecting boundary conditions are used along the walls of the tunnel. Inflow boundary conditions are imposed at the left end of the tunnel, and at the right, all of the gradients are

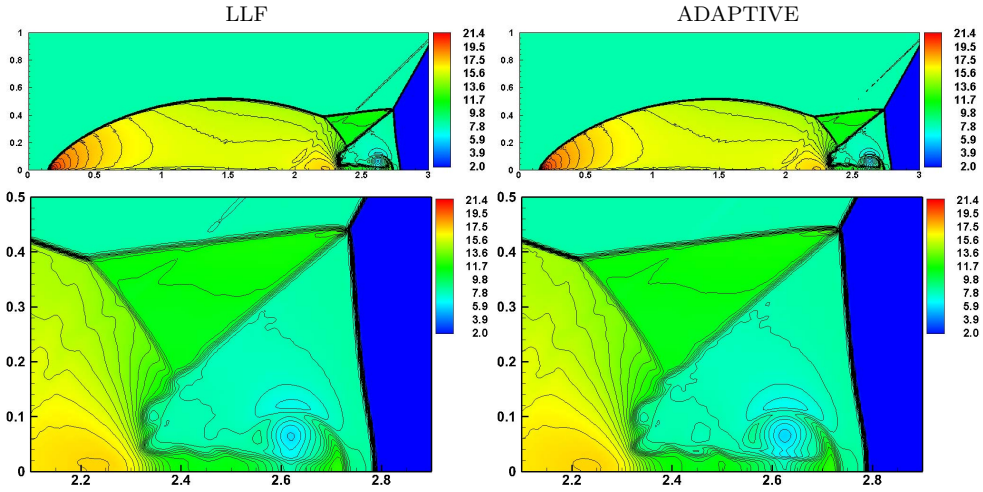

FIG. 5.12. *Example 6: Density (ρ) computed using the LLF (left column) and ADAPTIVE (right column) fluxes in the entire computational domain (top row) and zoom at the small structure area (bottom row).*

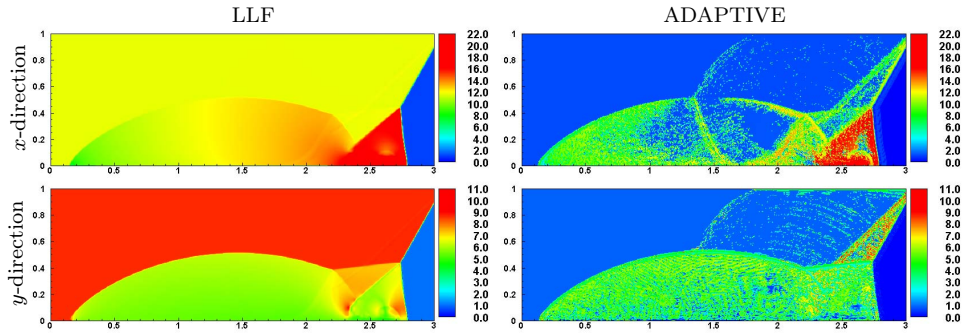

FIG. 5.13. *Example 6: ND coefficients in the x-direction (top row) and y-direction (bottom row) of the LLF (left column) and ADAPTIVE (right column) fluxes. Notice that the maximum values of the ND coefficients in the x- and y-directions are different as shown in the colormaps.*

assumed to vanish. Initially, the wind tunnel is filled with a gas with $\rho(x, y, 0) \equiv 1.4$, $p(x, y, 0) \equiv 1$, $u(x, y, 0) \equiv 3$, and $v(x, y, 0) \equiv 0$. The corner of the step is the center of a rarefaction fan and hence is a singular point of the flow. For the treatment of the singularity at the corner of the step, we adopt the same technique used in [48], which is based on the assumption of a nearly steady flow in the region near the corner.

We compute the ADAPTIVE and LLF solutions until the final time $t = 4$ on a uniform mesh with $\Delta x = \Delta y = 1/320$ and present the contour lines of the computed densities in Figure 5.14. As one can see, the vortical structures emulated along the slip line are much stronger and less diffused with the ADAPTIVE fluxes than the LLF ones. The ND coefficients of the ADAPTIVE fluxes are once again much smaller than the corresponding ND coefficients of the LLF fluxes, as shown in Figure 5.15. Most noticeably, along the unstable slip line emerging from the triple point along the shock front, which is responsible for the appearance of the small vortices due to the Kelvin–Helmholtz instabilities, the adaptive ND coefficients of the ADAPTIVE flux

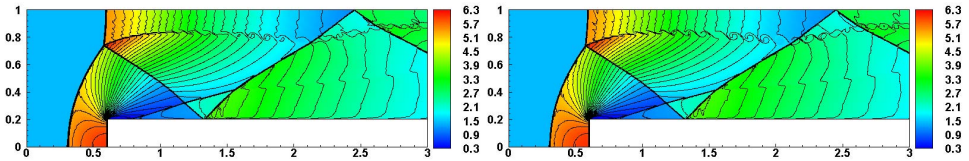

FIG. 5.14. *Example 7: Density (ρ) computed using the LLF (left) and ADAPTIVE (right) fluxes.*

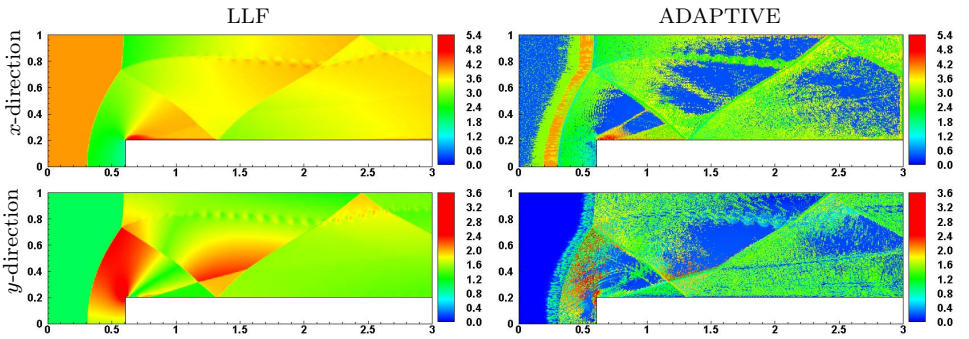

FIG. 5.15. *Example 7: ND coefficients in the x-direction (top row) and y-direction (bottom row) of the LLF (left column) and ADAPTIVE (right column) fluxes. Notice that the maximum values of the ND coefficients in the x- and y-directions are different as shown in the colormaps.*

are about a third smaller than the corresponding ND coefficients of the LLF flux. This allows the propagation of the vortices with smaller dissipation and thus the integrity of their shape is much better maintained downstream.

Example 8—Two-dimensional Riemann problem. In this example, we consider Configuration 3 of the 2-D Riemann problems from [28]; see also [30, 40, 41, 50]. The initial conditions are

$$(\rho(x,y,0),u(x,y,0),v(x,y,0),p(x,y,0)) = \begin{cases} (1.5,0,0,1.5), & x>0.8,\ y>0.8,\\ (0.5323,1.206,0,0.3), & x<0.8,\ y>0.8,\\ (0.138,1.206,1.206,0.029), & x<0.8,\ y<0.8,\\ (0.5323,0,1.206,0.3), & x>0.8,\ y<0.8. \end{cases}$$

We compute the ADAPTIVE and LLF solutions until the final time $t = 0.8$ on a uniform mesh with $\Delta x = \Delta y = 1/400$. The obtained densities are shown in Figure 5.16. As one can see, the large-scale structures of the flow, including the triple point, incident shock, reflected shock, Mach stem, and slip plane, are much better resolved when the proposed adaptive diffusion central numerical flux is used. Also, the instability along the neck of the jet is more pronounced in the ADAPTIVE solution with a stronger vorticity deposition there. The ND coefficients of both the ADAPTIVE and LLF fluxes are shown in Figure 5.17.

Example 9—Rayleigh–Taylor instability. In the last example, we consider the Rayleigh–Taylor instability problem taken from [42]. In this test, we numerically solve the compressible Euler equations with gravitation, which, in the case of acceleration due to gravity being set to $g = 1$, read as

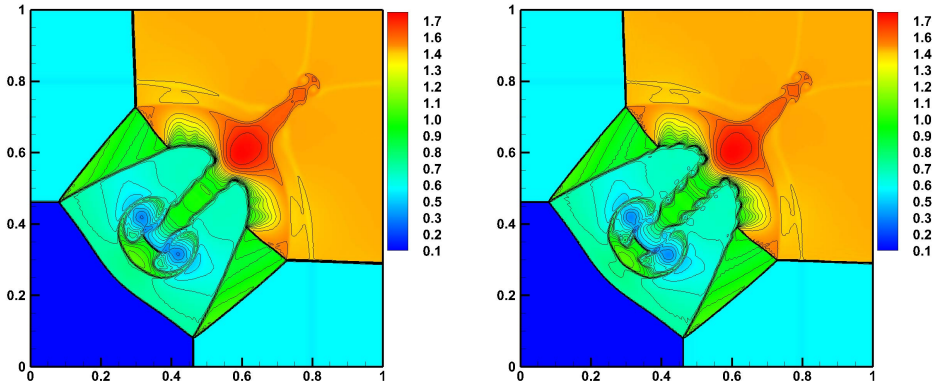

FIG. 5.16. *Example 8: Density (ρ) computed using the LLF (left) and ADAPTIVE (right) fluxes.*

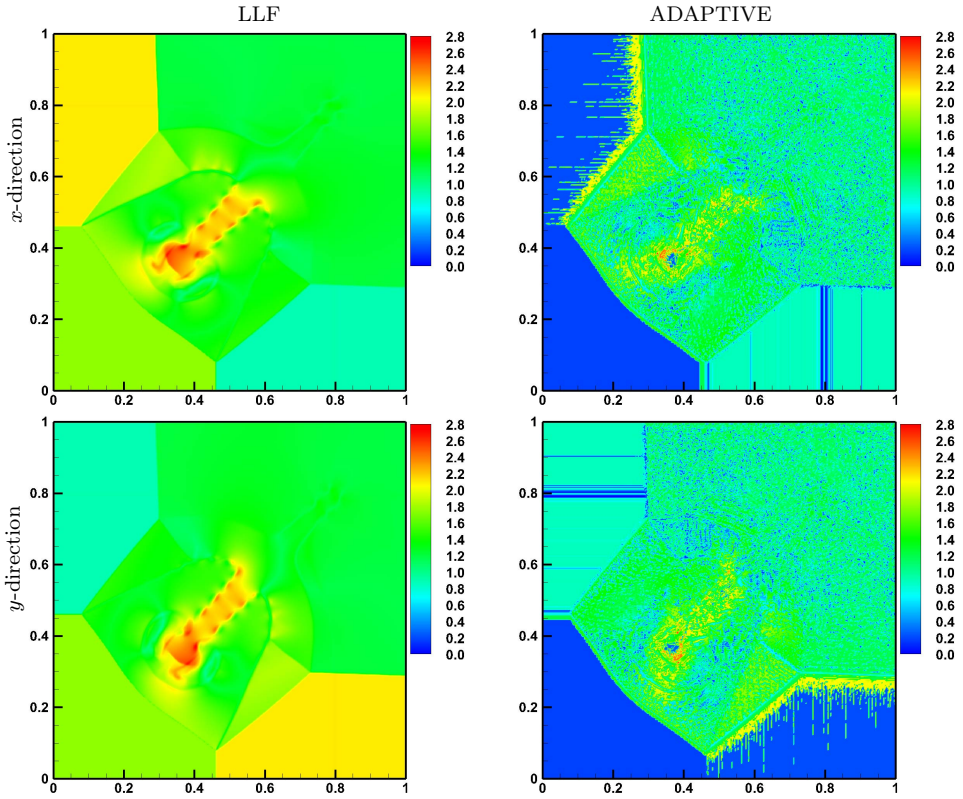

FIG. 5.17. *Example 8: ND coefficients in the x-direction (top row) and y-direction (bottom row) of the LLF (left column) and ADAPTIVE (right column) fluxes.*

$$\rho_t + (\rho u)_x + (\rho v)_y = 0,$$
$$m_t + (\rho u^2 + p)_x + (\rho uv)_y = 0,$$
$$n_t + (\rho uv)_x + (\rho v^2 + p)_y = \rho,$$
$$E_t + ((E+p)u)_x + ((E+p)v)_y = n.$$

The gravitational terms on the RHS are discretized straightforwardly, as explained in Remark 4.

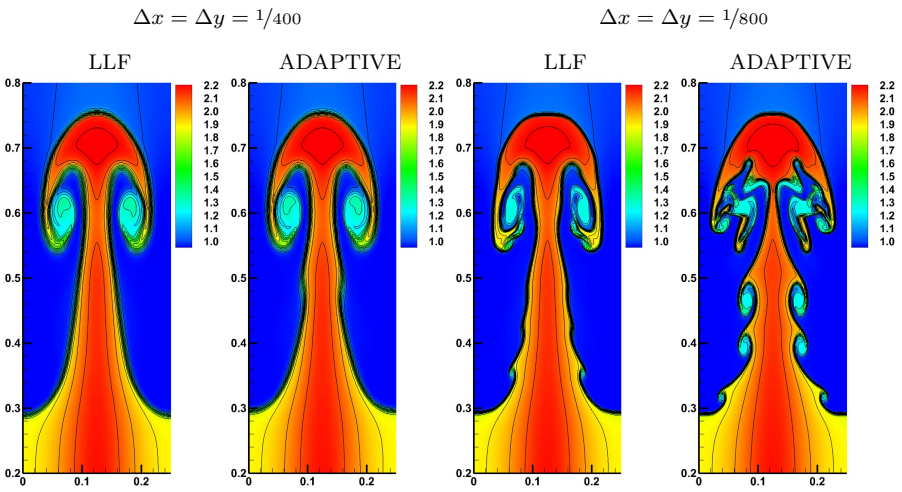

FIG. 5.18. *Example 9: Density (ρ) computed using the LLF and ADAPTIVE fluxes on two different grids.*

The computational domain is $[0, 0.25] \times [0, 1]$ and the initial conditions are

$$(\rho, u, v, p)\Big|_{(x,y,0)} = \begin{cases} (2, 0, -0.025\, c\cos(8\pi x), 2y + 1), & c = \sqrt{\frac{\gamma p}{\rho}} = \sqrt{\frac{5}{3}\left(y + \frac{1}{2}\right)}, \quad y < 0.5, \\ (1, 0, -0.025\, c\cos(8\pi x), y + 1.5), & c = \sqrt{\frac{\gamma p}{\rho}} = \sqrt{\frac{5}{3}\left(y + \frac{3}{2}\right)}, \quad y > 0.5. \end{cases}$$

Reflective boundary conditions are imposed at the left and right boundaries and the following Dirichlet boundary conditions are set at the top and bottom boundaries: $(\rho, u, v, p)\big|_{y=1} = (1, 0, 0, 2.5)$ and $(\rho, u, v, p)\big|_{y=0} = (2, 0, 0, 1)$.

In order to preserve the initial symmetry of the solution about the $x = 0.125$ axis, we follow [8] and symmetrize the initial y-velocity as follows:

$$v(x, y, 0) = \begin{cases} -0.025\, c\cos(8\pi x), & x < 0.125, \\ -0.025\, c\cos(8\pi(0.25 - x)), & x > 0.125. \end{cases}$$

In addition, the symmetry is enforced during the computation. This is done as follows: as soon as we compute certain values $\overline{\boldsymbol{U}}_\ell$ and $\overline{\boldsymbol{U}}_m$ such that $x_\ell + x_m = 0.25$, we replace these values with $\overline{\boldsymbol{U}}_\ell^*$ and $\overline{\boldsymbol{U}}_m^*$ computed according to Algorithm B.1 described in Appendix B.

We compute the ADAPTIVE and LLF solutions until the final time $t = 1.95$ on two different grids with $\Delta x = \Delta y = 1/400$ and $1/800$. The obtained densities are presented in Figure 5.18. As one can see (especially looking at finer mesh solutions), the use of smaller ND coefficients in the ADAPTIVE flux (see Figure 5.19) leads to a substantially higher resolution of the small complex structures.

6. Conclusion. One of the major drawbacks of higher-order nonlinear numerical schemes for the system of hyperbolic conservation laws is related to the fact that they often employ very diffusive numerical fluxes to suppress oscillations that appear in the areas where the solution contains large gradients and discontinuities. WENO schemes, which achieve a high order of accuracy with the help of high-order WENO interpolation procedures, often employ the robust, yet highly diffusive LLF numerical flux. In this work, we have developed an adaptive diffusion central numerical flux,

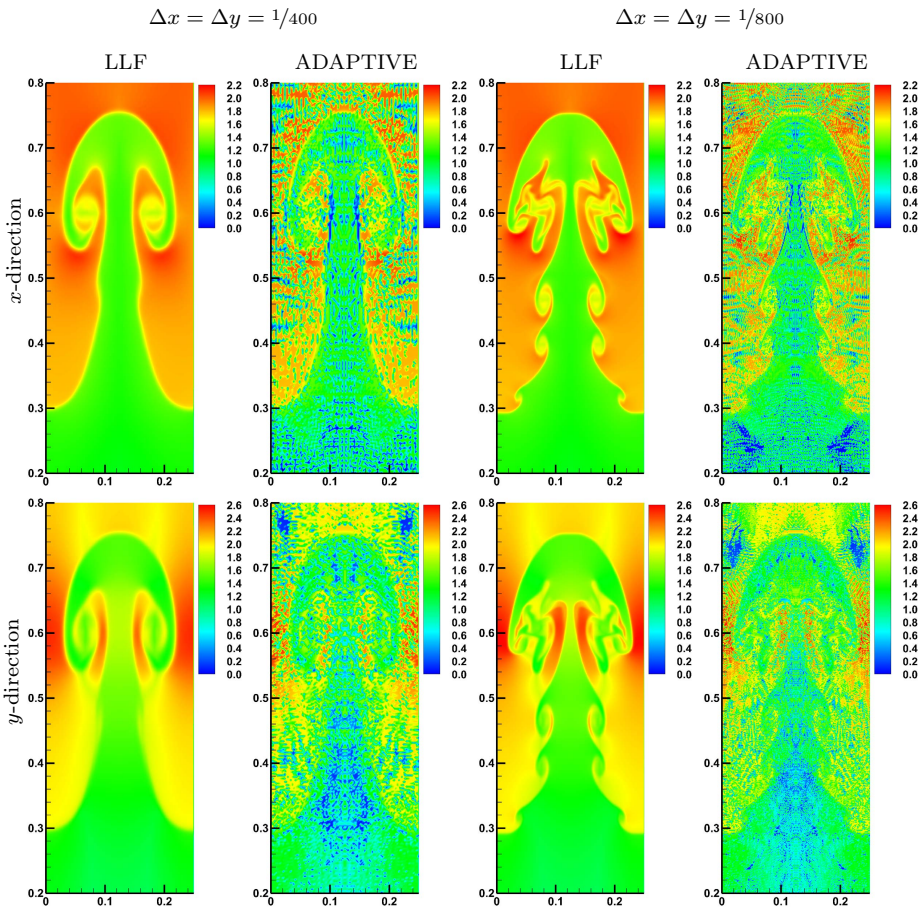

FIG. 5.19. *Example 9: ND coefficients in the x- (top row) and y-directions (bottom row) of the LLF (first and third columns) and ADAPTIVE (second and fourth columns) fluxes on two different grids. Notice that the maximum values of the ND coefficients in the x- and y-directions are different as shown in the colormaps.*

which is then implemented in the framework of a fifth-order A-WENO finite-difference scheme. The new flux can be viewed as a low diffusion modification of the LLF flux, whose ND coefficient is modified to allow an adaptive control on the amount of the ND based on the maximum local speed of propagation at the given location and time moment. The local speed of propagation is estimated using a suitable discrete version of the R-H condition. For adaptivity, lower and upper bounds of the adaptive ND coefficient are obtained using the C-P splitting of the Jacobian. In the regions where the solution is smooth, the upper bound is scaled down to remove the excessive ND. In the areas of large gradients and discontinuities, the ND coefficients may become as large as those of the LLF flux to suppress spurious oscillations and ensure robustness and the essentially nonoscillatory nature of the resulting fifth-order A-WENO scheme.

Our adaptive approach leads to an improved resolution of contact waves and fine-scale structures of the solutions, as demonstrated on a number of challenging 1-D and 2-D benchmarks. The obtained results suggest that the proposed adaptive diffusion central numerical flux outperforms the LLF flux, while being as robust as its more

diffusive counterpart. We have also compared the time evolution of the ND coefficients of both of the studied fluxes. The obtained results suggest that the ND coefficients can be substantially reduced without risking spurious oscillations wherever and whenever the computed solution is sufficiently smooth.

In this study, the proposed adaptive diffusion numerical flux has been implemented in the context of a fifth-order A-WENO finite-difference scheme applied to the Euler equations of gas dynamics. However, it can also be used as a numerical flux in the frameworks of finite-volume and discontinuous Galerkin methods. The resulting schemes can be applied to a variety of hyperbolic systems of conservation and balance laws, which will be a subject of our future research.

Appendix A. Convection-pressure flux splitting. In this section, we briefly review the C-P flux splitting proposed in [49].

It is well-known that for smooth solutions the compressible Euler system (3.3) is equivalent to the following quasi-linear system:

$$\boldsymbol{U}_t + A\,\boldsymbol{U}_x = \boldsymbol{0},$$

where the Jacobian is

$$A = \frac{\partial \boldsymbol{F}}{\partial \boldsymbol{U}} = \begin{pmatrix} 0 & 1 & 0 \\ \dfrac{\gamma-3}{2}u^2 & (3-\gamma)u & \gamma-1 \\ -\dfrac{c^2u}{\gamma-1} + \dfrac{\gamma-2}{2}u^3 & \dfrac{c^2}{\gamma-1} - \dfrac{2\gamma-3}{2}u^2 & \gamma u \end{pmatrix}.$$

The matrix A has three real and distinct eigenvalues $\lambda_1 = u-c < \lambda_2 = u < \lambda_3 = u+c$, and the corresponding right eigenvectors

$$\boldsymbol{r}_1 = \begin{pmatrix} 1 \\ u-c \\ H-uc \end{pmatrix}, \quad \boldsymbol{r}_2 = \begin{pmatrix} 1 \\ u \\ \frac{1}{2}u^2 \end{pmatrix}, \quad \boldsymbol{r}_3 = \begin{pmatrix} 1 \\ u+c \\ H+uc \end{pmatrix},$$

where $H := (E+p)/\rho$ is the enthalpy. A is diagonalizable and

$$A = R\Lambda R^{-1}, \tag{A.1}$$

where

$$\Lambda = \begin{pmatrix} u-c & 0 & 0 \\ 0 & u & 0 \\ 0 & 0 & u+c \end{pmatrix} \quad \text{and} \quad R = \begin{pmatrix} 1 & 1 & 1 \\ u-c & u & u+c \\ H-uc & \frac{1}{2}u^2 & H+uc \end{pmatrix}.$$

The C-P flux splitting is based on the following splitting of the diagonal matrix Λ into its convective ($\Lambda^{\rm c}$) and pressure ($\Lambda^{\rm p}$) parts:

$$\Lambda = \Lambda^{\rm c} + \Lambda^{\rm p}, \quad \Lambda^{\rm c} = \begin{pmatrix} u & 0 & 0 \\ 0 & u & 0 \\ 0 & 0 & u \end{pmatrix}, \quad \Lambda^{\rm p} = \begin{pmatrix} -c & 0 & 0 \\ 0 & 0 & 0 \\ 0 & 0 & c \end{pmatrix},$$

which can be substituted into (A.1) to obtain the corresponding splitting of the Jacobian:

$$A = A^{\rm c} + A^{\rm p}, \quad \text{where} \quad A^{\rm c} := R\Lambda^{\rm c}R^{-1} = \Lambda^{\rm c} \quad \text{and} \quad A^{\rm p} := R\Lambda^{\rm p}R^{-1}. \tag{A.2}$$

It is easy to show that the Jacobian splitting (A.2) leads to the following C-P flux splitting:

$$\boldsymbol{F}(\boldsymbol{U}) = A\,\boldsymbol{U} = (A^{\mathrm{c}} + A^{\mathrm{p}})\,\boldsymbol{U} = \boldsymbol{F}^{\mathrm{c}}(\boldsymbol{U}) + \boldsymbol{F}^{\mathrm{p}}(\boldsymbol{U}), \tag{A.3}$$

where

$$\boldsymbol{F}^{\mathrm{c}}(\boldsymbol{U}) = \begin{pmatrix} \rho u \\ \rho u^2 \\ Eu \end{pmatrix} \quad \text{and} \quad \boldsymbol{F}^{\mathrm{p}}(\boldsymbol{U}) = \begin{pmatrix} 0 \\ p \\ pu \end{pmatrix}.$$

Appendix B. Symmetrization algorithm.

Algorithm B.1 Symmetrization algorithm.

for $i = 1, 3, 4$ **do**

$A_i := \big(\overline{U}_\ell^{(i)} + \overline{U}_m^{(i)}\big)/2$

$B_i := \big(\overline{U}_m^{(i)} + \overline{U}_\ell^{(i)}\big)/2$

$C_i := \big(\max(A_i, B_i) + \min(A_i, B_i)\big)/2$

$\overline{U}_\ell^{*,(i)} := C_i$

$\overline{U}_m^{*,(i)} := \overline{U}_\ell^{*,(i)}$

end for

$A_2 := \big(|\overline{U}_\ell^{(2)}| + |\overline{U}_m^{(2)}|\big)/2$

$B_2 := \big(|\overline{U}_m^{(2)}| + |\overline{U}_\ell^{(2)}|\big)/2$

$C_2 := \big(\max(A_2, B_2) + \min(A_2, B_2)\big)/2$

$\overline{U}_\ell^{*,(2)} := C_2 \operatorname{sign}\big(\overline{U}_\ell^{(2)}\big)$

$\overline{U}_m^{*,(2)} := -\overline{U}_\ell^{*,(2)}$

REFERENCES

[1] D. S. Balsara, S. Garain, and C.-W. Shu, *An efficient class of WENO schemes with adaptive order*, J. Comput. Phys., 326 (2016), pp. 780–804.

[2] D. S. Balsara and C.-W. Shu, *Monotonicity preserving weighted essentially non-oscillatory schemes with increasingly high order of accuracy*, J. Comput. Phys., 160 (2000), pp. 405–452.

[3] M. Ben-Artzi and J. Falcovitz, *Generalized Riemann Problems in Computational Fluid Dynamics*, Cambridge Monogr. Appl. Comput. Math. 11, Cambridge University Press, Cambridge, UK, 2003.

[4] R. Borges, M. Carmona, B. Costa, and W. S. Don, *An improved weighted essentially non-oscillatory scheme for hyperbolic conservation laws*, J. Comput. Phys., 227 (2008), pp. 3191–3211.

[5] M. Castro, B. Costa, and W. S. Don, *High order weighted essentially non-oscillatory WENO-Z schemes for hyperbolic conservation laws*, J. Comput. Phys., 230 (2011), pp. 1766–1792.

[6] W. S. Don and R. Borges, *Accuracy of the weighted essentially non-oscillatory conservative finite difference schemes*, J. Comput. Phys., 250 (2013), pp. 347–372.

[7] W. S. Don, D.-M. Li, Z. Gao, and B.-S. Wang, *A characteristic-wise alternative WENO-Z finite difference scheme for solving the compressible multicomponent non-reactive flows in the overestimated quasi-conservative form*, J. Sci. Comput., 82 (2020), 27.

[8] N. Fleischmann, S. Adami, and N. A. Adams, *Numerical symmetry-preserving techniques for low-dissipation shock-capturing schemes*, Comput. Fluids, 189 (2019), pp. 94–107.

[9] Z. Gao, L.-L. Fang, B.-S. Wang, Y. Wang, and W. S. Don, *Seventh and ninth orders alternative WENO finite difference schemes for hyperbolic conservation laws*, Comput. Fluids, 202 (2020), 104519.

[10] N. K. Garg, S. V. Raghurama Rao, and M. Sekhar, *Weak-strong hyperbolic splitting for simulating conservation laws*, Int. J. Adv. Eng. Sci. Appl. Math., 7 (2015), pp. 62–69.
[11] E. Godlewski and P.-A. Raviart, *Numerical Approximation of Hyperbolic Systems of Conservation Laws*, Appl. Math. Sci. 118, Springer-Verlag, New York, 1996.
[12] S. K. Godunov, *A difference method for numerical calculation of discontinuous solutions of the equations of hydrodynamics*, Mat. Sb. (N.S.), 47 (1959), pp. 271–306.
[13] S. Gottlieb, D. Ketcheson, and C.-W. Shu, *Strong Stability Preserving Runge-Kutta and Multistep Time Discretizations*, World Scientific, Hackensack, NJ, 2011.
[14] S. Gottlieb, C.-W. Shu, and E. Tadmor, *Strong stability-preserving high-order time discretization methods*, SIAM Rev., 43 (2001), pp. 89–112.
[15] A. Harten, B. Engquist, S. Osher, and S. R. Chakravarthy, *Uniformly high-order accurate essentially nonoscillatory schemes.* III, J. Comput. Phys., 71 (1987), pp. 231–303.
[16] A. Harten and S. Osher, *Uniformly high-order accurate nonoscillatory schemes.* I, SIAM J. Numer. Anal., 24 (1987), pp. 279–309.
[17] A. K. Henrick, T. D. Aslam, and J. M. Powers, *Mapped weighted essentially non-oscillatory schemes: Achieving optimal order near critical points*, J. Comput. Phys., 207 (2005), pp. 542–567.
[18] J. S. Hesthaven, *Numerical Methods for Conservation Laws: From Analysis to Algorithms*, Comput. Sci. Eng. 18, SIAM, Philadelphia, 2018.
[19] S. Jaisankar and S. V. Raghurama Rao, *A central Rankine-Hugoniot solver for hyperbolic conservation laws*, J. Comput. Phys., 228 (2009), pp. 770–798.
[20] G.-S. Jiang and C.-W. Shu, *Efficient implementation of weighted ENO schemes*, J. Comput. Phys., 126 (1996), pp. 202–228.
[21] Y. Jiang, C.-W. Shu, and M. Zhang, *An alternative formulation of finite difference weighted ENO schemes with Lax-Wendroff time discretization for conservation laws*, SIAM J. Sci. Comput., 35 (2013), pp. A1137–A1160.
[22] D. Kröner, *Numerical Schemes for Conservation Laws*, Wiley-Teubner Ser. Adv. Numer. Math., John Wiley & Sons, Chichester, UK, 1997.
[23] A. Kurganov, *Central Schemes: A powerful black-box solver for nonlinear hyperbolic PDEs*, in Handbook of Numerical Methods for Hyperbolic Problems, Handb. Numer. Anal. 17, Elsevier/North-Holland, Amsterdam, 2016, pp. 525–548.
[24] A. Kurganov, *Finite-volume schemes for shallow-water equations*, Acta Numer., 27 (2018), pp. 289–351.
[25] A. Kurganov and G. Petrova, *A third-order semi-discrete genuinely multidimensional central scheme for hyperbolic conservation laws and related problems*, Numer. Math., 88 (2001), pp. 683–729.
[26] A. Kurganov and G. Petrova, *A second-order well-balanced positivity preserving central-upwind scheme for the Saint-Venant system*, Commun. Math. Sci., 5 (2007), pp. 133–160.
[27] A. Kurganov and E. Tadmor, *New high-resolution central schemes for nonlinear conservation laws and convection-diffusion equations*, J. Comput. Phys., 160 (2000), pp. 241–282.
[28] A. Kurganov and E. Tadmor, *Solution of two-dimensional Riemann problems for gas dynamics without Riemann problem solvers*, Numer. Methods Partial Differential Equations, 18 (2002), pp. 584–608.
[29] P. D. Lax, *Weak solutions of nonlinear hyperbolic equations and their numerical computation*, Comm. Pure Appl. Math., 7 (1954), pp. 159–193.
[30] P. D. Lax and X.-D. Liu, *Solution of two-dimensional Riemann problems of gas dynamics by positive schemes*, SIAM J. Sci. Comput., 19 (1998), pp. 319–340.
[31] R. J. LeVeque, *Finite Volume Methods for Hyperbolic Problems*, Cambridge Texts in Appl. Math., Cambridge University Press, Cambridge, UK, 2002.
[32] P. Li, W. S. Don, and Z. Gao, *High order well-balanced finite difference WENO interpolation-based schemes for shallow water equations*, Comput. Fluids, 201 (2020), 104476.
[33] H. Liu, *A numerical study of the performance of alternative weighted ENO methods based on various numerical fluxes for conservation law*, Appl. Math. Comput., 296 (2017), pp. 182–197.
[34] H. Liu and J. Qiu, *Finite difference Hermite WENO schemes for conservation laws,* II*: An alternative approach*, J. Sci. Comput., 66 (2016), pp. 598–624.
[35] X.-D. Liu, S. Osher, and T. Chan, *Weighted essentially non-oscillatory schemes*, J. Comput. Phys., 115 (1994), pp. 200–212.
[36] H. Nessyahu and E. Tadmor, *Nonoscillatory central differencing for hyperbolic conservation laws*, J. Comput. Phys., 87 (1990), pp. 408–463.
[37] J. Qiu and C.-W. Shu, *On the construction, comparison, and local characteristic decomposition for high-order central WENO schemes*, J. Comput. Phys., 183 (2002), pp. 187–209.

[38] S. V. Raghurama Rao and K. Balakrishna, *An accurate shock capturing algorithm with a relaxation system for hyperbolic conservation laws*, in Proceedings of the 16th AIAA Computational Fluid Dynamics Conference, 2003.
[39] V. V. Rusanov, *The calculation of the interaction of non-stationary shock waves with barriers*, Ž. Vyčisl. Mat. i Mat. Fiz., 1 (1961), pp. 267–279.
[40] C. W. Schulz-Rinne, *Classification of the Riemann problem for two-dimensional gas dynamics*, SIAM J. Math. Anal., 24 (1993), pp. 76–88.
[41] C. W. Schulz-Rinne, J. P. Collins, and H. M. Glaz, *Numerical solution of the Riemann problem for two-dimensional gas dynamics*, SIAM J. Sci. Comput., 14 (1993), pp. 1394–1394.
[42] J. Shi, Y.-T. Zhang, and C.-W. Shu, *Resolution of high order WENO schemes for complicated flow structures*, J. Comput. Phys., 186 (2003), pp. 690–696.
[43] C.-W. Shu, *High order weighted essentially nonoscillatory schemes for convection dominated problems*, SIAM Rev., 51 (2009), pp. 82–126.
[44] C.-W. Shu and S. Osher, *Efficient implementation of essentially non-oscillatory shock-capturing schemes*, J. Comput. Phys., 77 (1988), pp. 439–471.
[45] C.-W. Shu and S. Osher, *Efficient implementation of essentially nonoscillatory shock-capturing schemes.* II, J. Comput. Phys., 83 (1989), pp. 32–78.
[46] V. A. Titarev and E. F. Toro, *Finite-volume WENO schemes for three-dimensional conservation laws*, J. Comput. Phys., 201 (2004), pp. 238–260.
[47] B.-S. Wang, P. Li, Z. Gao, and W. S. Don, *An improved fifth order alternative WENO-Z finite difference scheme for hyperbolic conservation laws*, J. Comput. Phys., 374 (2018), pp. 469–477.
[48] P. Woodward and P. Colella, *The numerical solution of two-dimensional fluid flow with strong shocks*, J. Comput. Phys., 54 (1988), pp. 115–173.
[49] G.-C. Zha and E. Bilgen, *Numerical solutions of Euler equations by using a new flux vector splitting scheme*, Internat. J. Numer. Methods Fluids, 17 (1993), pp. 115–144.
[50] Y. Zheng, *Systems of Conservation Laws: Two-Dimensional Riemann Problems*, Progr. Nonlinear Differential Equations Appl. 38, Birkhäuser Boston, Boston, MA, 2001.